Orientation-controlled epitaxy of CoSn anisotropic conductive thin films on sapphire substrates toward interconnect applications

Tomoya Nakatani,[1*] Rohit Dahule,[2] Nattamon Suwannaharn,[2] Mevhibe Dilara Pütkül,[1] Yusuke Ikeda,[1] Taisuke T. Sasaki,[2] and Ryoji Sahara,[2]

[1] Research Center for Magnetic and Spintronic Materials, National Institute for Materials Science, 1-2-1, Sengen, Tsukuba, Ibaraki 305-0047, Japan.

[2] Research Center for Structural Materials, National Institute for Materials Science, 1-2-1, Sengen, Tsukuba, Ibaraki 305-0047, Japan.

[*]Corresponding author's email address: nakatani.tomoya@nims.go.jp

Abstract

The increasing resistivity of Cu interconnects at reduced device dimensions requires alternative conductors with suppressed size effects of resistivity. Materials with highly anisotropic electronic transport are a promising solution. CoSn exhibits pseudo-one-dimensional transport along the *c* axis with low resistivity comparable to conventional metals, making it a promising candidate for next-generation interconnects. In this study, we investigate the epitaxial growth of CoSn thin films on sapphire substrates with controlled crystallographic orientations to align the low-resistivity *c* axis in the plane. We successfully grow single-crystalline CoSn$(10\bar{1}0)$ and CoSn$(11\bar{2}0)$ films on sapphire substrates using appropriate buffer layers. Although the $(11\bar{2}0)$ plane has a higher atomic packing density and is thus expected to yield lower surface energy and smoother films based on an analogy with conventional metals, the two orientations show markedly different surface morphologies: CoSn $(10\bar{1}0)$ forms comparatively smooth films, whereas CoSn$(11\bar{2}0)$ exhibits pronounced $\{10\bar{1}0\}$-faceting and rough surfaces. First-principles calculations reveal that the $(10\bar{1}0)$ surface has lower surface energy than the $(11\bar{2}0)$ surface, consistent with the experimentally observed facet formation. This demonstrates that surface energetics in CoSn are governed not by atomic packing density but by anisotropic bonding associated with the kagome lattice. Electrical transport measurements confirm strong dependence of resistivity on crystallographic orientation, consistent with the bulk properties, with the lowest resistivity achieved along the *c* axis, down to 10.6 μΩ cm for 50-nm-thick CoSn$(10\bar{1}0)$. This work establishes orientation-controlled epitaxy on 300-mm-wafer-compatible sapphire substrates as a viable strategy for integrating CoSn into next-generation interconnect architectures.

I. Introduction

As transistor dimensions continue to shrink, the electrical resistivity (ρ) of conventional copper (Cu) interconnects increases significantly due to enhanced electron scattering at surfaces and grain boundaries.[1–3] This size effect originates from Cu's nearly isotropic Fermi surface and long electron mean free path ($\lambda \approx 39$ nm at room temperature).[4] Consequently, electron scattering at surfaces and grain boundaries is greatly increased in devices with small dimensions. To address this issue, materials with a small $\rho_0\lambda$ product (ρ_0: bulk resistivity) have been proposed, including platinum-group elements such as Ru.[5,6] Furthermore, materials exhibiting anisotropic electronic conduction have emerged as promising candidates because their transport can be engineered by crystallographic orientation.[7,8] Candidate materials include delafossites[9,10] and the CoSn kagome metal.[7]

CoSn crystallizes in a hexagonal B35 structure (hP6, space group P6/mmm), as illustrated in Fig. 1(a), exhibiting highly anisotropic, pseudo-one-dimensional transport. This property originates from its unique electronic band structure, which features a "flat band" formed by the destructive interference of the wave function of conduction electrons in the kagome lattice (*c* plane). While the resistivity in the *c* plane is high (> 100 μΩ cm), the resistivity is remarkably low along the [0001] *c* axis (3–7 μΩ cm in bulk [11–15]), making CoSn a promising candidate for next-generation interconnects.[7] In our previous study of single-crystalline CoSn$(10\bar{1}0)$ films with an in-plane *c* axis, two critical challenges were identified.[16] First, the measured *c* axis resistivity of down to 13 μΩ cm remained higher than the bulk value, suggesting additional scattering sources for conduction electrons, such as defects or impurities. Second, the CoSn $(10\bar{1}0)$ films exhibited three-

dimensional island growth, resulting in rough surfaces that are not suitable for device integration. These issues highlight the need for improved epitaxial growth to realize smooth and high-quality CoSn films.

For interconnect applications of CoSn, aligning the low-resistivity *c* axis parallel to the longitudinal direction of the interconnect line and the current direction is essential. Such alignment is difficult to achieve using polycrystalline films. To take advantage of the anisotropic electronic conduction of CoSn in a multilevel interconnect structure, the horizontal interconnects in each wiring layer must be patterned from a single-crystalline CoSn film as straight lines parallel to its *c* axis. A potential solution is the "wafer transfer" process, in which a single-crystalline CoSn film is grown on a template wafer and then transferred to a device-fabricated wafer. Then, the template wafer is removed (debonded), and the transferred CoSn film is patterned into interconnect lines. To implement this in modern semiconductor manufacturing, epitaxial CoSn growth must be established on 300-mm-wafer-compatible substrates, which are currently limited to Si, SiC, and sapphire (α-Al_2O_3).

Sapphire is a suitable substrate for the epitaxial growth of various materials and the wafer transfer process due to its high mechanical, thermal, and chemical stability, as well as its optical transparency to various wavelengths of light, including UV. Moreover, the variety of available crystal planes in sapphire offers significant flexibility in epitaxial design. In general, the choice of crystal plane strongly influences the epitaxial growth and surface morphology of the material, which are linked to crystal symmetry and surface energy. For growing single-crystalline CoSn films with an in-plane *c* axis, two epitaxial planes are possible: the $(10\bar{1}0)$ *M*-plane and the $(11\bar{2}0)$ *A*-plane. As illustrated in Figs.

1(b) and 1(c), the $(11\bar{2}0)$ plane has a higher atomic packing density (10.3 atoms/nm^2) than the $(10\bar{1}0)$ plane (8.9 atoms/nm^2).

In simple metals with isotropic bonding, surface energy is well approximated by the density of broken bonds and thus correlates with atomic packing density.[17] Therefore, densely packed planes generally have lower surface energy and tend to form flatter surfaces in thin films. Based on this analogy, one may expect that CoSn$(11\bar{2}0)$ epitaxy would be favorable for achieving smoother films with an in-plane *c* axis compared to CoSn$(10\bar{1}0)$. However, CoSn is a kagome metal with intrinsically anisotropic bonding associated with its anisotropic crystal structure. In such systems, surface energetics may not be solely governed by atomic packing density because the number and nature of broken bonds can vary significantly depending on the crystallographic orientation. Therefore, a more detailed investigation of orientation-dependent growth and surface morphology is required.

In this study, we investigate the epitaxial growth of CoSn single-crystalline films on sapphire substrates. We demonstrate the growth of both CoSn$(10\bar{1}0)$ and $(11\bar{2}0)$ films and systematically analyze how the crystallographic plane influences the surface morphology, microstructure, and electronic transport properties. This study aims to establish a viable pathway for integrating single-crystalline CoSn films into next-generation interconnect technologies.

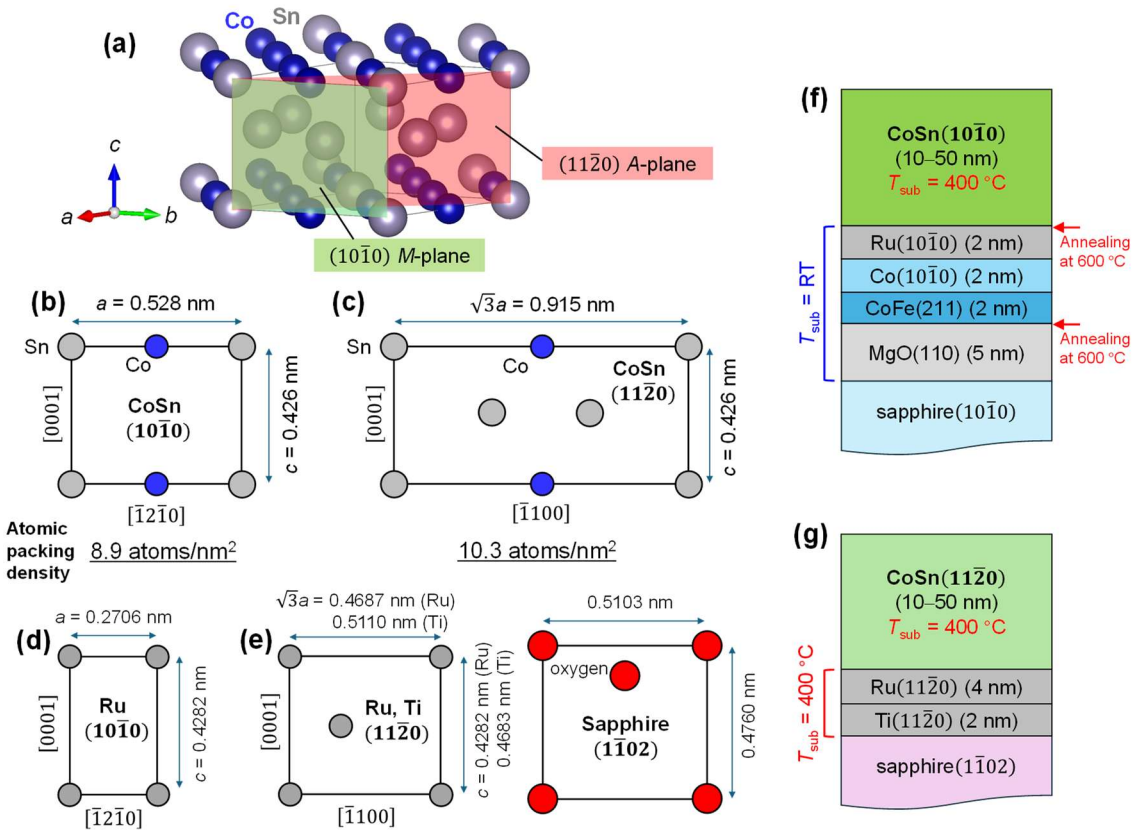


FIG. 1. (a) Crystal structure of the kagome metal CoSn. (b) $(10\bar{1}0)$ and (c) $(11\bar{2}0)$ planes of CoSn, representing the two candidate epitaxial planes for achieving in-plane *c* axis orientation. (d) Atomic arrangement of the Ru $(10\bar{1}0)$ plane. (e) Atomic arrangements of the Ru$(11\bar{2}0)$ and Ti$(11\bar{2}0)$, along with the oxygen sublattice of the sapphire $(1\bar{1}02)$ *R*-plane. Schematic sample structures for (f) CoSn $(10\bar{1}0)$ and (g) CoSn$(11\bar{2}0)$ epitaxial growth.

II. Methods

(i) Experiments

All thin-film samples were deposited using magnetron sputtering in an Ar gas atmosphere. The base pressure of the deposition chamber was ~2×10^{-6} Pa. As illustrated in Figs. 1(b) and 1(d), the $(10\bar{1}0)$ planes of CoSn and Ru exhibit good lattice matching,

with mismatch ratios of –0.5% along $[0001]$ and –2.5% along $[\bar{1}2\bar{1}0]$ relative to the Ru lattice. Therefore, Ru$(10\bar{1}0)$ is a suitable template for growing CoSn$(10\bar{1}0)$. To achieve this epitaxy, we used sapphire$(10\bar{1}0)$ (*M*-plane) substrates and a complex buffer architecture consisting of the following layers, from the substrate side: MgO(110) (5 nm)/$Co_{50}Fe_{50}$(211) (2 nm)/Co$(10\bar{1}0)$ (2 nm)/Ru$(10\bar{1}0)$ (2 nm), as shown in Fig. 1(f). As reported by Talvacchio et al.[18] and Stampe et al.,[19] MgO(110) grows epitaxially on sapphire$(10\bar{1}0)$ with an orientation relationship of $[1\bar{1}0]_{\mathrm{MgO}} \parallel [0001]_{\mathrm{sapphire}}$. First, the sapphire substrate was cleaned by heating it in the sputtering chamber at 600 °C for 10 min. The MgO layer was deposited by RF sputtering of a sintered MgO target at room temperature (RT) and subsequently annealed at 600 °C for 10 min in the sputtering chamber to improve the crystallinity of the MgO(110) single-crystalline film, which is critical for the epitaxy of the overlying metallic layers. After depositing the Ru buffer layer, a second annealing step was performed at 600 °C for 10 min, resulting in improved crystal quality of the subsequent CoSn layer. The CoSn layers were co-sputtered from elemental Co and Sn targets at a substrate temperature of 400 °C. The stoichiometry ($Co_{50}Sn_{50}$ at. %) was precisely controlled within ±1% to ensure the phase purity of CoSn, as previously described.[16]

For CoSn $(11\bar{2}0)$ films, sapphire $(1\bar{1}02)$ (*R*-plane) substrates were used. Similar to the $(10\bar{1}0)$ plane, the $(11\bar{2}0)$ planes of Ru and CoSn exhibit good lattice matching, as shown in Figs. 1(c) and (e). However, Ru$(11\bar{2}0)$ could not be epitaxially grown on sapphire $(1\bar{1}02)$ owing to the large lattice mismatch of –10.0% along $[0001]_{\mathrm{Ru}}$ and –8.2% along $[\bar{1}100]_{\mathrm{Ru}}$ between the oxygen sublattice of sapphire$(1\bar{1}02)$ and Ru$(11\bar{2}0)$. Therefore, we first deposited a Ti$(11\bar{2}0)$ (2 nm) layer at 400 °C on

sapphire($1\bar{1}02$), exhibiting small lattice mismatch ratios of –1.6% along $[0001]_{Ti}$ and +0.1% along $[\bar{1}100]_{Ti}$. Then, a Ru (4 nm) buffer layer was deposited at 400 °C. Despite the relatively large lattice mismatch ratios of –8.6% and –8.3% along $[0001]$ and $[\bar{1}100]$, respectively, the $(11\bar{2}0)$-plane epitaxy between Ti and Ru was obtained.

We characterized the crystal structure using X-ray diffraction (XRD) with Cu K_α radiation and the microstructure using scanning transmission electron microscopy (STEM). Surface morphologies were evaluated via atomic force microscopy (AFM). We measured the resistivity of the CoSn epitaxial thin films using a four-probe method in patterned devices with a width of 50 μm and a length of 100 μm, using a combination of photolithography and Ar ion milling. As previously reported, resistance measurements in unpatterned films using an in-line four-probe method yield inaccurate sheet resistance values for materials with resistivity anisotropy.[16]

(ii) Computational details

First-principles calculations were performed within the framework of density functional theory (DFT), as implemented in the Vienna Ab initio Simulation Package (VASP).[20,21] The Perdew-Burke-Ernzerhof generalized gradient approximation (PBE-GGA) was adopted for the exchange-correlation functional,[22] together with the projector augmented-wave (PAW) method.[23] The valence electron configurations considered were $3d^8 4s^1$ for Co and $5s^2 5p^2$ for Sn. A plane-wave kinetic energy cutoff of 450 eV was used for all calculations. The bulk structure was fully optimized prior to surface construction using a Γ-centered 10×10×11 Monkhorst-Pack *k*-point mesh for Brillouin zone integration.[24] The optimized lattice parameters of CoSn are a = 0.529 nm and c = 0.422

nm, which are close to the experimental values (a = 0.528 nm and c = 0.426 nm).[25] Electronic self-consistency was achieved with a convergence criterion of 10^{-6} eV, and the force convergence threshold was set to 0.01 eV/Å.

Surface slabs for the (0001), $(10\bar{1}0)$ and $(11\bar{2}0)$ orientations were constructed from the optimized bulk structure. Each slab naturally exposes two opposing planes, (0001) and (0002), $(10\bar{1}0)$ and $(20\bar{2}0)$, and $(11\bar{2}0)$ and $(22\bar{4}0)$ arising from the bulk stacking sequence. A five-layer slab geometry was employed along the surface normal, separated by a vacuum region of 15 Å to prevent spurious interactions between periodically repeated images (see Fig. S3). The atoms in the bottom two layers were fixed to mimic bulk-like behavior, while the upper three layers were allowed to fully relax. Dipole corrections were applied along the surface normal to eliminate artificial electrostatic interactions.[26] Brillouin zone integration for the surface calculations was performed using Γ-centered k-point meshes of 10×10×1 for (0001), $(10\bar{1}0)$ surfaces and 6×10×1 for $(11\bar{2}0)$ surface.

Surface energies were evaluated using a two-step approach involving cleavage and relaxation contributions.[27] The cleavage energy, E_{cleavage}, was calculated from the unrelaxed slab as

$$E_{\mathrm{cleavage}} = \frac{1}{2A}[E_{\mathrm{slab}}^{\mathrm{unrelax}} - N \times E_{\mathrm{bulk}}], \qquad (1)$$

where $E_{\mathrm{slab}}^{\mathrm{unrelax}}$ is the total energy of the unrelaxed slab, E_{bulk} is the energy of the bulk reference structure, N is the number of bulk formula units contained in the slab and A is surface area. Structural relaxation of the upper layers then provided the relaxation energy, $E_{\mathrm{relaxation}}$,

$$E_{\mathrm{relaxation}} = \frac{1}{A}[E_{\mathrm{slab}}^{\mathrm{relax}} - E_{\mathrm{slab}}^{\mathrm{unrelax}}], \qquad (2)$$

where $E_{\mathrm{slab}}^{\mathrm{relax}}$ is the total energy of the relaxed slab. The total surface energy, $\gamma_{\mathrm{surface}}$, is obtained as

$$\gamma_{\mathrm{surface}} = E_{\mathrm{cleavage}} + E_{\mathrm{relaxation}}. \quad (3)$$

III. Results

A. Crystal structures and surface morphology of CoSn$(10\bar{1}0)$

First, we describe the growth of CoSn$(10\bar{1}0)$ on the sapphire$(10\bar{1}0)$ via the MgO(110)/CoFe(211)/Co$(10\bar{1}0)$/Ru$(10\bar{1}0)$ buffer system. For comparison, the same buffer layers and CoSn films were deposited on an MgO(110) substrate. Figure 2(a) shows the out-of-plane XRD profiles of a 10-nm-thick MgO film on sapphire$(10\bar{1}0)$ in both as-deposited and annealed states. In both cases, only the MgO 220 peak was observed, confirming the out-of-plane alignment of the (110)-plane of MgO. The annealing process at 600 °C clearly increased the peak intensity, indicating improved MgO crystallinity. The inset of Fig. 2(a) shows the ϕ-scan profile of the MgO 200 reflections at 2θ = 42.9° with a χ tilt of 45°; the twofold symmetry confirms that MgO(110) grows as a single crystal with the orientation relationship of $[1\bar{1}0]_{\mathrm{MgO}} \parallel [0001]_{\mathrm{sapphire}}$ as reported previously.[18,19]

Figure 2(b) shows the out-of-plane XRD profiles for 50-nm-thick CoSn films grown on both MgO(110) and sapphire$(10\bar{1}0)$ substrates via MgO (5 nm)/CoFe (2 nm)/Co (2 nm)/Ru (2 nm) buffer layers. The presence of the CoSn $10\bar{1}0$ reflection and its higher-order peaks indicates a preferred out-of-plane alignment of CoSn$(10\bar{1}0)$. However, as shown in Fig. 2(b), the CoSn 0002 peak at 2θ = 42.0° was observed only for the film on the sapphire substrate, suggesting the presence of misoriented grains in the

film. Figure 2(c) shows the ϕ-scan profiles of the CoSn $11\bar{2}0$ reflections, where the twofold symmetry confirms the single-crystalline growth of CoSn with the relationship of $[0001]_{\mathrm{sapphire}} \parallel [1\bar{1}0]_{\mathrm{MgO}} \parallel [\bar{1}2\bar{1}0]_{\mathrm{CoSn}}$. The t_{CoSn}-dependence of the full width at half maximum (FWHM) for the rocking curves of the CoSn $10\bar{1}0$ reflection along the β-axis [inset of Fig. 2(b)] and ϕ-axis (Fig. 2(c)]is summarized in Fig. 2(d). The β-axis corresponds to the azimuthal coordinate of the diffraction spot on the two-dimensional detector, where $\beta = 180°$ is defined as the surface normal direction. Therefore, the FWHM along the β-axis reflects the tilt distribution of the corresponding crystallographic planes, i.e., the CoSn$(10\bar{1}0)$ planes in the present case. For the same sample, the FWHM measured along the β-axis is approximately 0.8° larger than that measured along the ω-axis due to the different optical configurations employed in these measurements. Therefore, the β-axis FWHMs in Figs. 2(d) and 3(d) are used to compare the relative evolution of crystalline alignment among the CoSn films. Although the FWHM values decrease with increasing t_{CoSn} for both substrates, the crystallinity of the CoSn films on sapphire substrates remains inferior to that on MgO(110) at any given thickness.

The surface morphology of the CoSn films was characterized by AFM, as shown in Figs. 2(e) and 2(f). For t_{CoSn} = 10 nm, the CoSn surface exhibits a three-dimensional island-like morphology (Fig. 2(e)). The peak-to-valley (p-v) values exceeded 20 nm, which is greater than the nominal film thickness of 10 nm, indicating that the islands are at least partially disconnected. For t_{CoSn} = 50 nm (Fig. 2(f)), the arithmetic average roughness (R_{a}) decreased, and the p-v values became smaller than the film thickness, suggesting the formation of a continuous film. Furthermore, the AFM images reveal that the surface grains are elongated along the c axis, suggesting a higher crystal growth

velocity along the *c* axis than the *a* axis.

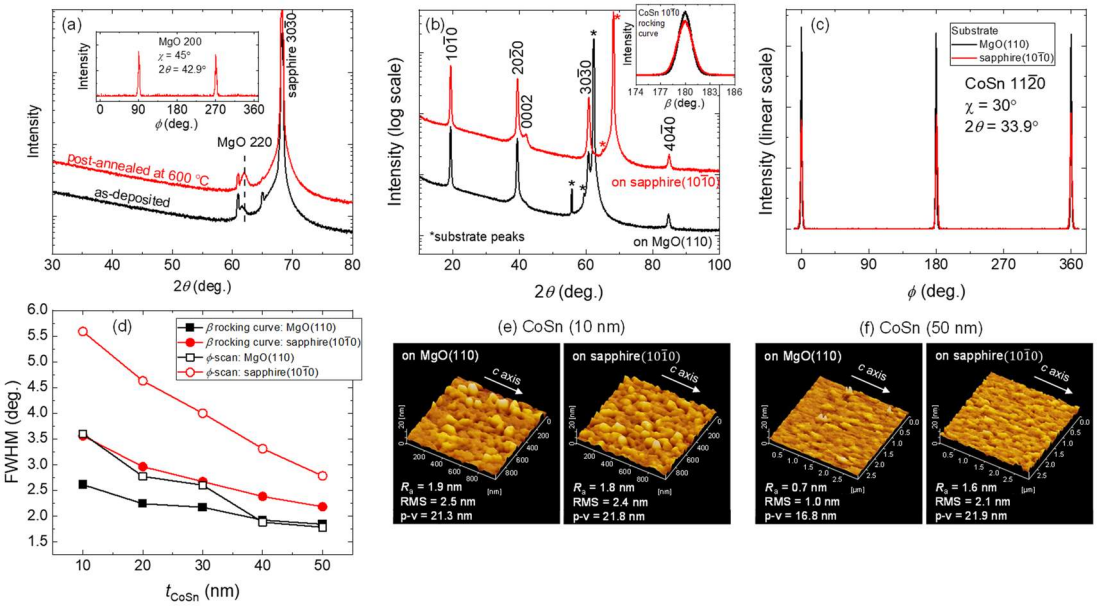


FIG. 2. Epitaxial growth of CoSn$(10\bar{1}0)$. (a) Out-of-plane XRD profiles of MgO (10 nm) on a sapphire$(10\bar{1}0)$ substrate. The inset shows ϕ-scan profile from the MgO 200 reflections. (b) Out-of-plane XRD profiles of MgO (5 nm)/CoFe (2 nm)/Co (2 nm)/Ru (2 nm)/CoSn (50 nm) films on MgO(110) and sapphire $(10\bar{1}0)$ substrates. The inset displays the rocking curve of CoSn $10\bar{1}0$ peak along the β-axis. (c) ϕ-scan profile of the CoSn $11\bar{2}0$ reflection. (d) t_{CoSn} dependence of the full width at half maximum (FWHM) of the rocking curves for the β and ϕ axes. AFM surface images of the CoSn films with thicknesses of (e) t_{CoSn} = 10 nm and (f) t_{CoSn} = 50 nm on MgO(110) and sapphire$(10\bar{1}0)$ substrates.

B. Crystal structures and surface morphology of CoSn$(11\bar{2}0)$

Next, we discuss the growth of CoSn$(11\bar{2}0)$ on the sapphire$(1\bar{1}02)$ substrate/Ti (2 nm)/Ru (4 nm) buffer system. Figure 3(a) shows a two-dimensional XRD image of a 50-nm-thick CoSn sample. As shown in Fig. 3(a) and the inset of Fig. 3(b), the CoSn $11\bar{2}0$ and $22\bar{4}0$ peaks, as well as the Ru $11\bar{2}0$ peak, are shifted from the surface normal (β = 180°) by approximately 1°. This indicates a tilt of the $(11\bar{2}0)$ planes of Ru and CoSn relative to the sapphire $(1\bar{1}02)$ substrate. The Ti $11\bar{2}0$ peak, which is expected to appear at 2θ = 62.6°, was not observed because the 2-nm-thick Ti layer was too thin to exhibit sufficient XRD intensity. To investigate this further, we prepared a separate 10-nm-thick Ti film on sapphire$(1\bar{1}02)$. The Ti $11\bar{2}0$ peak appeared exactly at β = 180° with a narrow FWHM of 0.7°, significantly smaller than that of Ru (FWHM = 2.9°) [inset of Fig. 3(b)]. These results confirm that Ti $(11\bar{2}0)$ grows with high crystallinity parallel to the substrate surface, as expected from the lattice matching between sapphire$(1\bar{1}02)$ and Ti$(11\bar{2}0)$ (Fig. 1(e)). Therefore, the $(11\bar{2}0)$ planes of Ru and CoSn are tilted by approximately 1° with respect to the underlying Ti$(11\bar{2}0)$ plane, most likely due to the 8.6% lattice mismatch between Ti and Ru.

Figures 3(b) and 3(c) show the out-of-plane XRD profiles and the ϕ-scan profiles of the CoSn $10\bar{1}0$ reflections, respectively. The twofold symmetry observed in the ϕ-scan confirms the single-crystalline growth of CoSn$(11\bar{2}0)$. As shown in Fig. 3(d), the crystallinity of CoSn improves with increasing t_{CoSn}, similar to the trend observed in the $(10\bar{1}0)$ films [Fig. 2(d)]. However, the surface morphology remained significantly rough. Figure 3(e) shows the AFM image and height (z-scale) line profile measured perpendicular to the c axis for t_{CoSn} = 10 nm. This reveals a highly directional morphology with sharp ridges oriented along the c axis, indicating a higher crystal growth velocity

along the *c* axis and pronounced facet growth. For t_{CoSn} = 50 nm [Fig. 3(f)], the surface exhibits flat terraces and deep voids with a p-v value of 71.4 nm, which exceeds the nominal film thickness. Contrary to our initial expectation based on the atomic packing density of CoSn$(10\bar{1}0)$ and $(11\bar{2}0)$ [Figs. 1(b) and 1(c)], the epitaxial growth of CoSn$(11\bar{2}0)$ failed to yield a flat surface and instead resulted in a rougher morphology than that of CoSn$(10\bar{1}0)$.

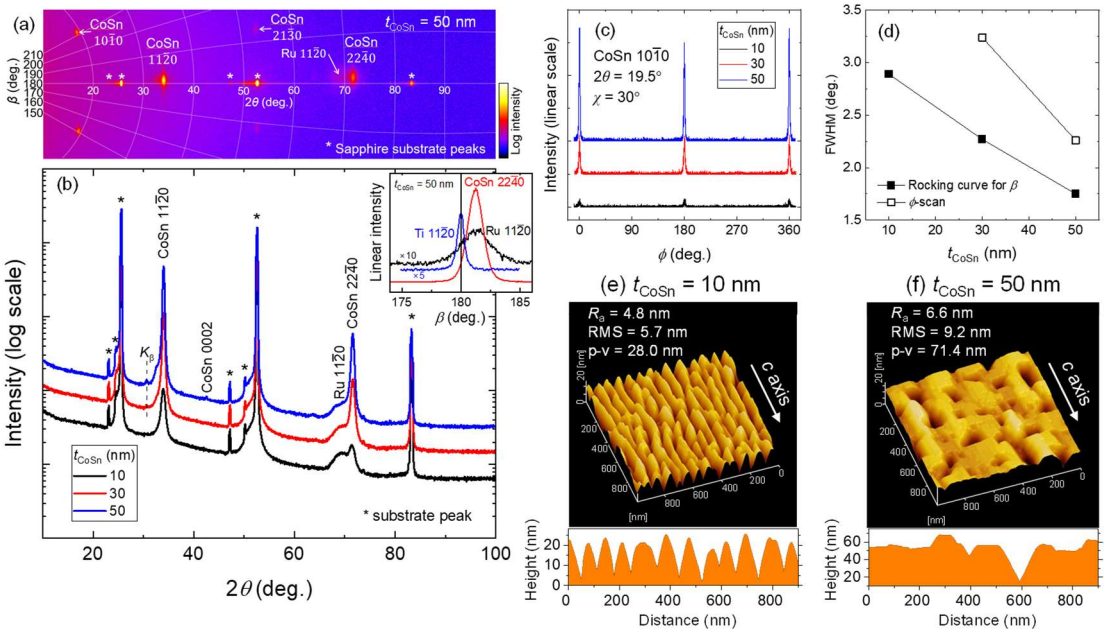


FIG. 3. Epitaxial growth of CoSn$(11\bar{2}0)$. (a) Two-dimensional (2D) XRD image of a CoSn$(11\bar{2}0)$ (t_{CoSn} = 50 nm) film on sapphire$(1\bar{1}02)$/Ti (2 nm)/Ru (4 nm). (b) Out-of-plane XRD profiles for t_{CoSn} = 10–50 nm, integrated from the 2D images over β = 175°–185°. The inset shows rocking curves of Ru $11\bar{2}0$ and CoSn $22\bar{4}0$ reflections along the β-axis. The rocking curve of the Ti $11\bar{2}0$ reflection from Ti (10 nm) on sapphire$(1\bar{1}02)$ is also shown. (c) ϕ-scan profile from the CoSn $10\bar{1}0$ reflection. (d) t_{CoSn} dependence of the FWHM of the rocking curves for the β and ϕ axes. AFM surface

images and height line profiles measured perpendicular to the *c* axis for (e) t_{CoSn} = 10 nm and (f) t_{CoSn} = 50 nm.

C. Microstructure

Figures 4(a) and 4(b) show low-magnification high-angle annular dark-field (HAADF)-STEM images of CoSn$(10\bar{1}0)$ films with t_{CoSn} = 10 and 50 nm grown on sapphire$(10\bar{1}0)$ substrates via MgO (5 nm)/CoFe (2 nm)/Co (2 nm)/Ru (2 nm) buffer layers. The images were taken along the [0001] zone axis (*c* axis) of CoSn. Since the contrast in HAADF-STEM images is approximately proportional to the square of the atomic number (Z^2), the bright thin layer corresponds to the 2-nm-thick Ru ($Z = 44$) buffer layer. Although the Ru buffer layer is relatively flat, the 10-nm-thick CoSn film exhibits a rough surface morphology, while the 50-nm-thick CoSn film appears relatively smooth. These observations are consistent with our previous report on CoSn$(10\bar{1}0)$ grown on MgO(110) substrates,[16] as well as with the reduced surface roughness observed in thicker samples via AFM measurements [Figs. 2(e) and 2(f)]. However, the Ru buffer layer appears faint or discontinuous in some regions, as indicated by an arrow in Fig. 4(b), although the CoSn$(10\bar{1}0)$ growth is still observed on top of these regions.

Figures 4(c) and 4(d) show the overlaid energy dispersive X-ray spectroscopy (EDS) elemental concentration maps of O, Mg, Co, Ru, and Pt (protective layer), together with the corresponding line profiles for the 10-nm-thick CoSn sample. In both samples, an approximately 3-nm-thick oxidized layer was observed on top of the CoSn film. The Co and Sn distributions within the CoSn layer remained relatively uniform and homogeneous, with no clear evidence of compositional fluctuation observed inside the

CoSn film. The broadening of the Ru concentration toward the CoFe buffer layer observed in the concentration line profile suggests that Ru has diffused partially into the Co and CoFe buffer layers, which may be related to the solid solubility of Ru and Co. This diffusion may also be related to the observed Fe segregation at the MgO/CoFe and Ru/CoSn interfaces. However, Ru diffusion into the CoSn layer was not detected. Similar EDS characteristics were also observed for the 50-nm-thick CoSn film. Oxygen was also detected inside the CoSn layer at around 20 at. %. Considering the presence of a 3-nm-thick oxidized layer on CoSn surface, similar passivated oxide layers may also form on the front and back surfaces of the TEM lamella after specimen preparation. Therefore, the measured oxygen concentration in the CoSn layer may be overestimated due to these passivation layers. X-ray photoelectron spectroscopy (XPS) measurements indicated that no significant oxygen signal was detected in the interior of the CoSn layer. [see Sec. 2 of the Supplementary Material]

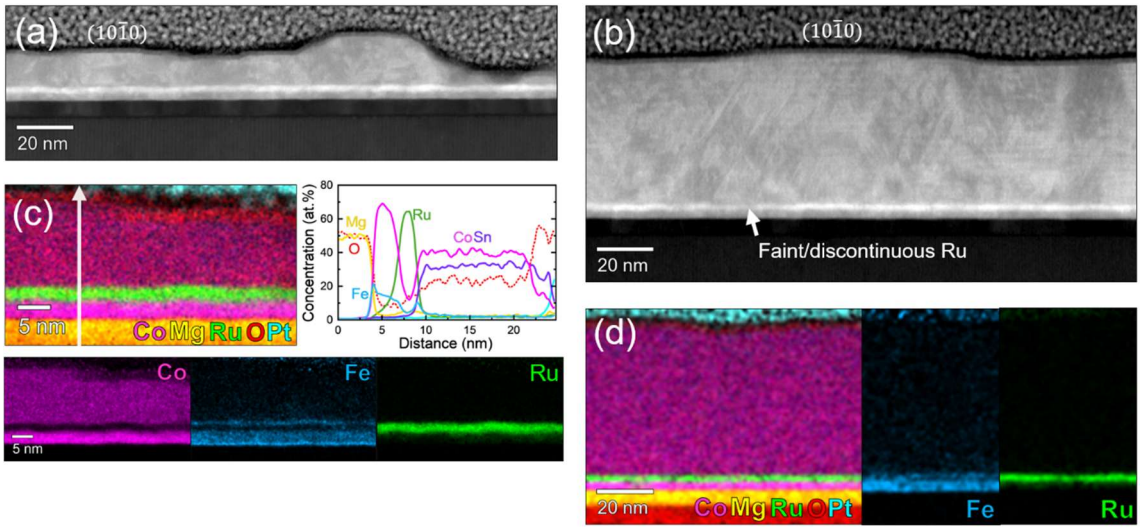


FIG. 4. HAADF-STEM images (a, b) and EDS elemental maps (c, d) of CoSn$(10\bar{1}0)$ films grown with nominal thicknesses of 10 and 50 nm, respectively, together with the corresponding EDS line profile for the 10-nm sample.

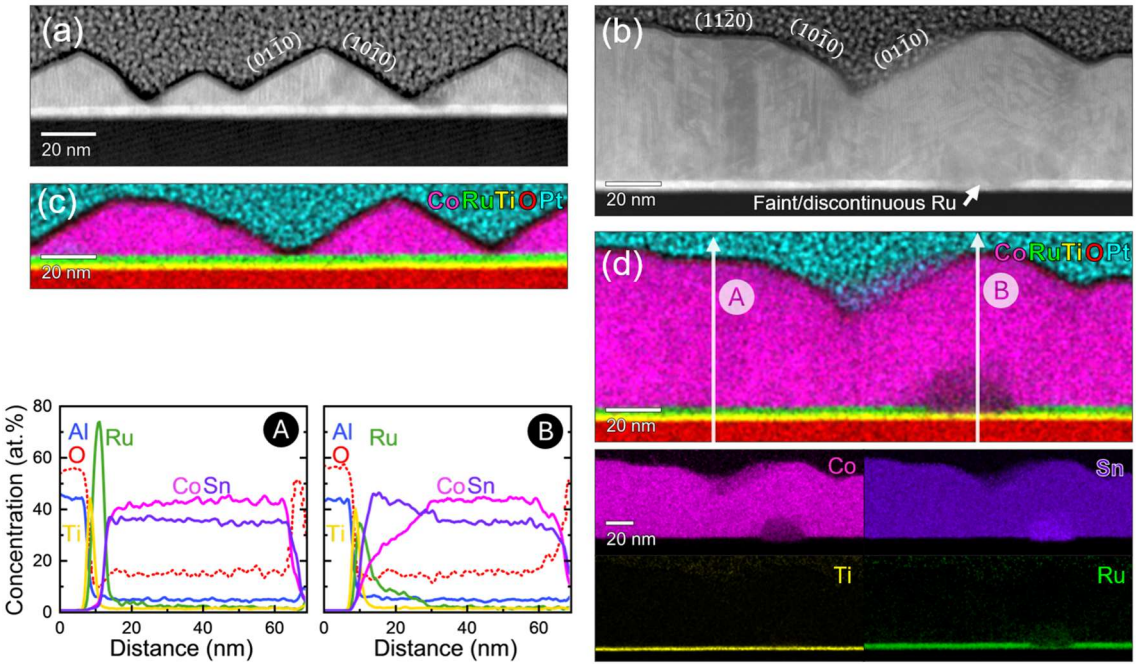


FIG. 5. HAADF-STEM images (a, b) and EDS elemental maps (c, d) of CoSn$(11\bar{2}0)$ films grown with thicknesses of 10 and 50 nm, respectively, together with the corresponding EDS line profiles for the 50-nm sample.

Figures 5(a) and 5(b) show HAADF-STEM images of CoSn$(11\bar{2}0)$ films with t_{CoSn} = 10 and 50 nm, respectively, grown on sapphire$(1\bar{1}02)$ substrates via Ti (2 nm)/Ru (4 nm) buffer layers. These images were taken along the [0001] zone axis of CoSn. The 10-nm-thick CoSn$(11\bar{2}0)$ film exhibited distinct facet growth, with isolated CoSn islands showing $\{10\bar{1}0\}$ facets. This is consistent with the AFM image, as shown in Fig. 3(e). In contrast, as the film thickness increased to 50 nm, the CoSn islands coalesced,

partially forming the designed $(11\bar{2}0)$ top facet. The bright contrast corresponding to the thin Ru buffer layer in the t_{CoSn} = 10 nm sample appeared relatively flat and continuous within the observed region. However, in the t_{CoSn} = 50 nm sample, the Ru buffer layer became discontinuous or faint in some regions.

EDS elemental maps of the 10-nm and 50-nm CoSn samples are shown in Figs. 5(c) and 5(d), respectively. While the elemental distributions of Co and Sn appeared relatively uniform in the 10-nm sample [Fig. 5(c)], elemental diffusion and compositional inhomogeneity were observed in the 50-nm sample [Fig. 5(d)]. Compared to region (A), region (B) exhibited Co depletion and Sn enrichment in areas above the Ru buffer layer. Ru diffusion into the CoSn film was also detected in these regions, which may be related to the solid solubility of Co and Ru, as shown in the EDS line profiles. Therefore, interdiffusion occurred in regions where the Ru layer was discontinuous.

As shown in Fig. 6 (a) and 6(b), high-magnification HAADF-STEM images clearly reveal the kagome structure along the [0001] zone axis for the 50-nm-thick CoSn$(10\bar{1}0)$ and CoSn$(11\bar{2}0)$ films, respectively. Despite their different growth orientations, domain boundaries were observed in both films. These domain boundaries exhibited similar structures and were aligned parallel to the $(10\bar{1}0)$ plane, similar to those previously reported for CoSn$(10\bar{1}0)$ films grown on MgO(110) substrates.[16] The identification of the structure of the domain boundaries requires STEM observations along another zone-axis and image-simulation studies. Therefore, detailed structural characterization of the domain boundaries and evaluation of their effect on electronic transport properties remain subjects for future study.

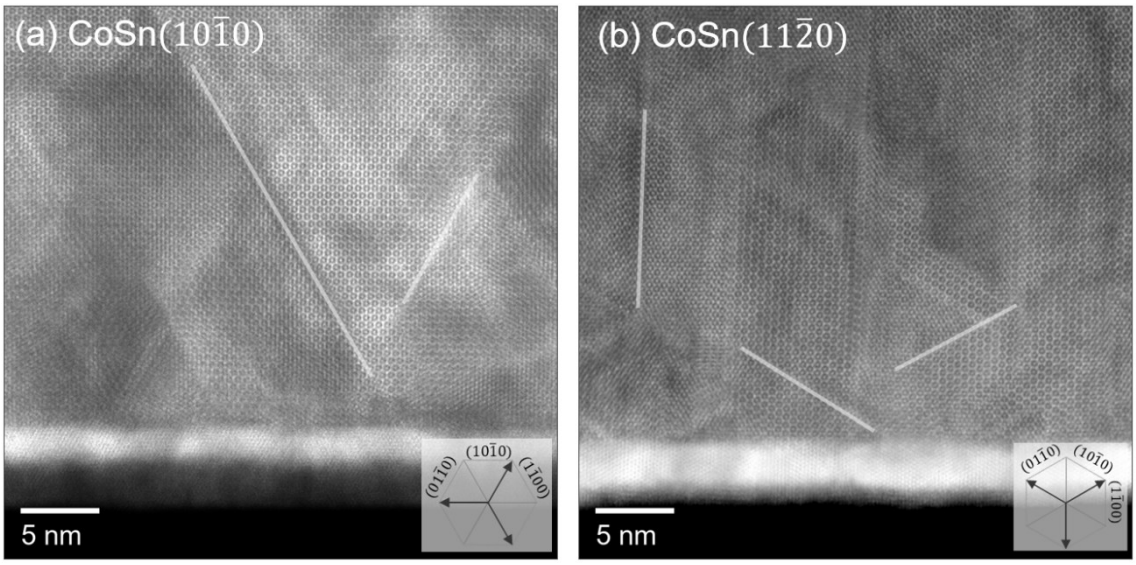


FIG. 6. High-magnification HAADF-STEM images of 50-nm-thick (a) CoSn$(10\bar{1}0)$ and (b) CoSn$(11\bar{2}0)$ films.

D. Anisotropic resistivity

The resistivity of the CoSn films (ρ^{CoSn}) was obtained as $\rho^{\mathrm{CoSn}} = t_{\mathrm{CoSn}}/(1/R_{\mathrm{s}}^{\mathrm{total}} - 1/R_{\mathrm{s}}^{\mathrm{buffer}})$, where $R_{\mathrm{s}}^{\mathrm{total}}$ and $R_{\mathrm{s}}^{\mathrm{buffer}}$ are the sheet resistances of the entire film and buffer layers, respectively, and t_{CoSn} is the nominal CoSn thickness determined from the pre-calibrated deposition rate and deposition time. This nominal thickness corresponds to the average film thickness for films with rough surface morphology. The method for estimating $R_{\mathrm{s}}^{\mathrm{buffer}}$ is described in the Supplementary Material. When calculating ρ^{CoSn}, we considered the errors of $R_{\mathrm{s}}^{\mathrm{total}}$, $R_{\mathrm{s}}^{\mathrm{buffer}}$, and t_{CoSn}. The combined error by $R_{\mathrm{s}}^{\mathrm{total}}$ and t_{CoSn} was 1.7%, while that of $R_{\mathrm{s}}^{\mathrm{buffer}}$ was much larger (see the Supplementary Material). The in-plane directions orthogonal to the low-resistivity *c* axis are $[\bar{1}2\bar{1}0]$ (*a* axis) and $[\bar{1}100]$ for the CoSn$(10\bar{1}0)$ and CoSn$(11\bar{2}0)$ films, respectively. In ideal

hexagonal crystal, hexagonal symmetry requires isotropic resistivity within the basal plane,[28] therefore, $\rho_{\parallel a}^{\mathrm{CoSn}} = \rho_{\parallel[\bar{1}100]}^{\mathrm{CoSn}} = \rho_{\parallel\mathrm{basal}}^{\mathrm{CoSn}}$.

Figure 7(a) shows the resistivity of CoSn$(10\bar{1}0)$ films with various t_{CoSn} values grown on MgO(110) and sapphire$(10\bar{1}0)$ substrates. For both substrates, the $\rho_{\parallel\mathrm{basal}}^{\mathrm{CoSn}}$ values were 100–140 μΩ cm for t_{CoSn} = 10–50 nm, consistent with the values in the bulk single crystals ($\rho_{\parallel\mathrm{basal}}^{\mathrm{CoSn}}$ ~120 μΩ cm).[13,15] The c axis resistivity ($\rho_{\parallel c}^{\mathrm{CoSn}}$) exhibited similar values for the MgO(110) and sapphire$(10\bar{1}0)$ substrates. As shown in Fig. 2(d), the CoSn films grown on the sapphire$(10\bar{1}0)$ substrate exhibited lower crystallinity than those grown on the MgO(110) substrate. However, the similar $\rho_{\parallel c}^{\mathrm{CoSn}}$ values on these substrates indicate that this degree of difference in the $(10\bar{1}0)$-crystallinity is not significant for $\rho_{\parallel c}^{\mathrm{CoSn}}$. The value of $\rho_{\parallel c}^{\mathrm{CoSn}}$ depends strongly on t_{CoSn}: $\rho_{\parallel c}^{\mathrm{CoSn}}$ = 10.6 μΩ cm for t_{CoSn} = 50 nm and $\rho_{\parallel c}^{\mathrm{CoSn}}$ ~30 μΩ cm for t_{CoSn} = 10 nm. However, since the CoSn surface roughness is more significant in thinner films due to the three-dimensional CoSn $(10\bar{1}0)$ growth, the observed $\rho_{\parallel c}^{\mathrm{CoSn}}$–$t_{\mathrm{CoSn}}$ relationship contains an extrinsic contribution from surface roughness. Therefore, we cannot evaluate the intrinsic dependence of $\rho_{\parallel c}^{\mathrm{CoSn}}$ on t_{CoSn} unless we achieve smooth CoSn film surfaces.

Figure 7(b) shows the resistivity of CoSn$(11\bar{2}0)$ films with different t_{CoSn} grown on a sapphire$(1\bar{1}02)$ substrate using Ti (2 nm)/Ru (4 nm) buffer layers. Similar to the CoSn$(10\bar{1}0)$ films, $\rho_{\parallel c}^{\mathrm{CoSn}}$ increased with decreasing t_{CoSn}. However, at a given t_{CoSn}, $\rho_{\parallel c}^{\mathrm{CoSn}}$ was higher for the CoSn $(11\bar{2}0)$ films than for the CoSn $(10\bar{1}0)$ films; for example, $\rho_{\parallel c}^{\mathrm{CoSn}}$ = 17.1 and 10.6 μΩ cm for 50-nm-thick CoSn$(11\bar{2}0)$ and CoSn$(10\bar{1}0)$, respectively. Similarly, at a given t_{CoSn}, $\rho_{\parallel\mathrm{basal}}^{\mathrm{CoSn}}$ was higher for the CoSn$(11\bar{2}0)$ films

than for the CoSn$(10\bar{1}0)$ films. These differences in resistivity between the two epitaxial orientations may arise from several structural factors. Domain boundaries with similar structures and apparently comparable densities within the observed regions were found in both films, as shown in Fig. 6. In addition, the CoSn$(10\bar{1}0)$ and CoSn$(11\bar{2}0)$ films exhibited comparable rocking-curve FWHMs at a given t_{CoSn}, as shown in Figs. 2(d) and 3(d). These observations suggest that neither domain-boundary scattering nor differences in the degree of crystalline alignment are likely to be the primary origin of the systematic resistivity difference.

In contrast, interdiffusion between Ru and CoSn was detected in the 50-nm-thick CoSn$(11\bar{2}0)$ film but not in the CoSn$(10\bar{1}0)$ films. This interdiffusion, together with the associated compositional inhomogeneity, may contribute to the higher resistivity of the 50-nm-thick CoSn$(11\bar{2}0)$ film. However, because such interdiffusion was not detected in the 10-nm-thick CoSn$(11\bar{2}0)$ film within the observation area for STEM, its contribution to the systematic resistivity difference between these epitaxial orientations cannot be determined from the present results.

The pronounced surface roughness of the CoSn$(11\bar{2}0)$ films due to the $\{10\bar{1}0\}$ facet growth may also contribute to the higher resistivity. In particular, the 10-nm-thick CoSn$(11\bar{2}0)$ consisted of $\{10\bar{1}0\}$-faceted islands elongated along the *c* axis [Figs. 3(e) and 5(a)]. This surface morphology may account for $\rho_{\parallel\mathrm{basal}}^{\mathrm{CoSn}}$ of ~206 μΩ cm, which is significantly higher than that for the 10-nm-thick CoSn$(10\bar{1}0)$ film (~110 μΩ cm). In addition, the 10-nm-thick CoSn$(11\bar{2}0)$ film exhibited nearly isolated islands with limited connectivity along the $[\bar{1}100]$ direction, whereas substantial island coalescence was observed in the 50-nm-thick films (Fig. 5). This thickness-dependent improvement

in film connectivity may partly explain the increasing $\rho_{\parallel\text{basal}}^{\text{CoSn}}$ with decreasing t_{CoSn} for the CoSn$(11\bar{2}0)$ films.

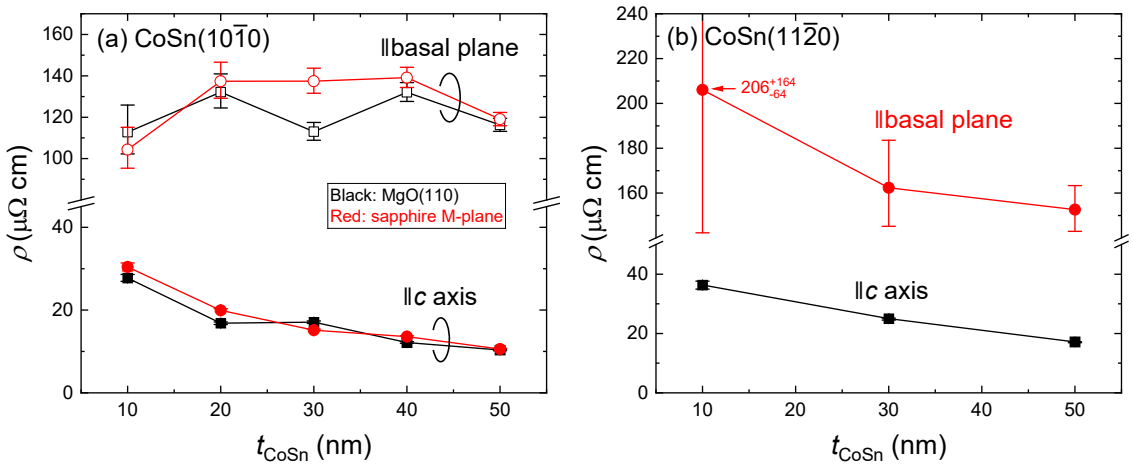


FIG. 7. t_{CoSn}-dependence of the resistivity of (a) CoSn$(10\bar{1}0)$ and (b) CoSn$(11\bar{2}0)$ films along the *c* axis and in the basal plane. The effect of the current shunting through the buffer layers has been subtracted.

IV. Discussion

The experimentally observed difference in surface morphology between the CoSn $(10\bar{1}0)$ and $(11\bar{2}0)$ single-crystalline films is counterintuitive from the viewpoint of conventional metallic thin films. In simple metals with nearly isotropic bonding, densely packed crystallographic planes generally exhibit lower surface energies and therefore tend to form flatter films. Because the CoSn$(11\bar{2}0)$ plane has a higher atomic packing density (10.3 atoms/nm^2) than the CoSn$(10\bar{1}0)$ plane (8.9 atoms/nm^2) [Figs. 1(b) and 1(c)], one would expect CoSn$(11\bar{2}0)$ epitaxy to produce smoother

surfaces. However, our experiments revealed the opposite trend: CoSn$(10\bar{1}0)$ forms comparatively smooth films, whereas CoSn$(11\bar{2}0)$ exhibits pronounced faceting and rough surfaces. This discrepancy clearly indicates that atomic packing density alone is insufficient to describe the surface stability in CoSn.

To clarify the origin of the observed surface morphology, we calculated the cleavage, relaxation, and total surface energies of representative CoSn surfaces using DFT. The results are summarized in Table 1. Except for the $(22\bar{4}0)$ surface, the relaxation energy associated with surface reconstruction did not significantly impact the surface energy [see Sec. 3 of the Supplementary Material]. The surface energy follows the sequence of (0001) < $(20\bar{2}0)$ < (0002) < $(10\bar{1}0)$ < $(22\bar{4}0)$ < $(11\bar{2}0)$. The (0001) surface (kagome plane) exhibits both the highest atomic packing density (14.3 atoms/nm^2) and the lowest surface energy. However, this correlation between atomic packing density and surface energy breaks down when comparing $(10\bar{1}0)$ and $(11\bar{2}0)$ surfaces, as well as $(20\bar{2}0)$ and $(22\bar{4}0)$ surfaces. This behavior suggests that the cleavage energy is primarily governed by the number and topology of broken Co-Sn, Co-Co, and Sn-Sn bonds associated with the kagome network rather than by atomic packing density alone. Consequently, crystallographic planes with relatively high atomic packing density do not necessarily have low surface energies in CoSn. Additional analyses of surface relaxation and charge redistribution are presented in the Supplementary Material.

It should be noted that surface energies alone do not determine the growth mode and surface morphology of sputtered CoSn thin films. Thin-film morphology can also be influenced by kinetic factors, such as adatom mobility and anisotropic growth rates, as well as by interface energy and elastic strain energy. Therefore, the present DFT results

should be interpreted as explaining the preferential expression of low-energy facets within the orientation-constrained epitaxial geometry, rather than providing a complete description of the growth mode of CoSn thin films.

Although the CoSn(0001) surface has the lowest surface energy, it is not the relevant top-surface orientation for the present films, in which either CoSn$(10\bar{1}0)$ or CoSn$(11\bar{2}0)$ is constrained to be parallel to the substrate surface, thereby aligning the *c* axis within the film plane. In addition, the elongated surface morphology observed by AFM suggests that crystal growth is faster along the *c* axis than along the transverse in-plane direction. Under this orientation constraint, the relevant comparison is between non-basal surfaces parallel to the *c* axis, namely, CoSn $(10\bar{1}0)$ and CoSn $(11\bar{2}0)$ surfaces.

At the elevated growth temperature of 400 °C employed in this study, sputtered adatoms are expected to have high surface mobility, which can promote aggregation and three-dimensional island growth. Once such island growth occurs, CoSn islands are expected to preferentially expose $\{10\bar{1}0\}$ facets because the calculated surface energy of CoSn$(10\bar{1}0)$ is lower than that of CoSn$(11\bar{2}0)$. This tendency is consistent with the preferential appearance of $\{10\bar{1}0\}$ facets observed experimentally in both CoSn$(10\bar{1}0)$ and CoSn$(11\bar{2}0)$ epitaxial films. With increasing thickness, these islands coalesce into a continuous film, resulting in a substantially smoother morphology, as observed for the CoSn$(10\bar{1}0)$ film with t_{CoSn} = 50 nm [Fig. 4(b)]. These results suggest that improving thin-film smoothness further will require suppressing facet-mediated island growth while maintaining the favorable CoSn$(10\bar{1}0)$ orientation that aligns the low-resistivity *c* axis within the film plane.

Table 1 Cleavage, relaxation and total surface energies (in eV Å^{-2}) of CoSn surfaces.

Surface	E_{cleavage}	$E_{\text{relaxation}}$	γ_{surface}
(0001)	0.080	–0.008	0.072
(0002)	0.080	–0.001	0.079
(10$\bar{1}$0)	0.087	–0.006	0.081
(20$\bar{2}$0)	0.087	–0.009	0.078
(11$\bar{2}$0)	0.105	–0.005	0.100
(22$\bar{4}$0)	0.105	–0.017	0.088

V. Conclusions

Single-crystalline CoSn $(10\bar{1}0)$ and $(11\bar{2}0)$ films were grown on sapphire $(10\bar{1}0)$ and $(1\bar{1}02)$ substrates using appropriate buffer architectures. CoSn$(10\bar{1}0)$ films initially exhibit three-dimensional island growth, leading to a rough surface at small thicknesses. With increasing thickness, the islands coalesce into a continuous film with improved surface flatness. A 50-nm-thick CoSn $(10\bar{1}0)$ film exhibits pronounced resistivity anisotropy, with $\rho_{\|c}^{\text{CoSn}}$ = 10.6 μΩ cm and $\rho_{\|\text{basal}}^{\text{CoSn}}$ = 120 μΩ cm, approaching the intrinsic anisotropic transport properties of bulk CoSn. In contrast, CoSn$(11\bar{2}0)$ films exhibit pronounced facet formation with $\{10\bar{1}0\}$ planes, resulting in significantly rougher surfaces and higher resistivity. First-principles calculations reveal that the $(10\bar{1}0)$ surface has a lower surface energy than the $(11\bar{2}0)$ surface. This explains the faceted growth behavior despite the higher atomic packing density of the $(11\bar{2}0)$ surface. These results demonstrate that the surface stability in CoSn is not governed by atomic packing density but rather by the anisotropic bonding characteristics of the kagome lattice.

These findings demonstrate that CoSn $(10\bar{1}0)$ epitaxy is the most suitable approach for achieving relatively smooth, single-crystalline films with the in-plane *c* axis orientation required for interconnect applications. This work provides design guidelines for the orientation-controlled growth of anisotropic conductors and emphasizes the critical role of surface energetics in determining film morphology and transport performance. To implement CoSn interconnects, future work should establish full-wafer epitaxy on 300-mm-compatible substrates together with a suitable sacrificial layer for wafer debonding, and develop compatible chemical mechanical polishing, wafer-bonding, and CoSn etching processes.

Acknowledgements

We acknowledge Kosuke Imamura and Mitsuru Ohtake (Yokohama National University) for valuable discussions. This work was supported by "JST-Research and Development Program for Next-generation Edge AI Semiconductors" Grant Number JPMJES2531. The XRD and XPS measurements were supported by ARIM of MEXT (JPMXP1225NM5220 and JPMXP1226NM5145). The computational results presented in this work were obtained using the Numerical Materials Simulator supercomputing facilities at NIMS.

Supplementary Material

Refer to the Supplementary Material for the method to estimate the buffer-layer sheet resistance, XPS data, and additional analyses of surface relaxation and charge redistribution based on DFT calculations.

Data Availability Statement

The data supporting the findings of this study are available from the corresponding author upon reasonable request.

Conflict of interest

The authors have no conflict of interest regarding the publication of this article.

References

[1] D. Gall, J.J. Cha, Z. Chen, H.J. Han, C. Hinkle, J.A. Robinson, R. Sundararaman, and R. Torsi, "Materials for interconnects," MRS Bull. **46**(10), 959–966 (2021).

[2] J.-P. Soulié, K. Sankaran, B. Van Troeye, A. Leśniewska, O. Varela Pedreira, H. Oprins, G. Delie, C. Fleischmann, L. Boakes, C. Rolin, L.-Å. Ragnarsson, K. Croes, S. Park, J. Swerts, G. Pourtois, Z. Tőkei, and C. Adelmann, "Selecting alternative metals for advanced interconnects," J. Appl. Phys. **136**, 171101 (2024).

[3] J.S. Kim, J. Kim, D.J. Yang, J. Shim, L. Hu, C.S. Lee, J. Kim, and S.W. Kim, "Addressing interconnect challenges for enhanced computing performance," Science **386**(6727), eadk6189 (2024).

[4] J.S. Chawla, and D. Gall, "Specular electron scattering at single-crystal Cu(001) surfaces," Appl. Phys. Lett. **94**, 252101 (2009).

[5] D. Gall, "Electron mean free path in elemental metals," J. Appl. Phys. **119**, 085101 (2016).

[6] S. Dutta, K. Sankaran, K. Moors, G. Pourtois, S. Van Elshocht, J. Bömmels, W. Vandervorst, Z. Tokei, and C. Adelmann, "Thickness dependence of the resistivity of platinum-group metal thin films," J. Appl. Phys. **122**, 025107 (2017).

[7] S. Kumar, C. Multunas, B. Defay, D. Gall, and R. Sundararaman, "Ultralow electron-surface scattering in nanoscale metals leveraging Fermi-surface anisotropy," Phys. Rev. Mater. **6**, 085002 (2022).

[8] K. Moors, K. Sankaran, G. Pourtois, and C. Adelmann, "First-principles-based screening method for resistivity scaling of anisotropic metals," Phys. Rev. Mater.

6(12), 123804 (2022).

[9] Y. Li, G. Zhou, M.M. Kelley, S. Shahriyar Nishat, S. Bey, M. Abdul Karim, X. Liu, B.A. Assaf, D. Gall, R. Sundararaman, and C.L. Hinkle, "PtCoO 2 for Scaled Interconnects," Small Struct. **2400638**, (2025).

[10] T. Harada, Z.P.L. Ang, Y. Sakakibara, T. Nagai, and Y. Masahiro, "Scalable alloy-based sputtering of high-conductivity PdCoO2 for advanced interconnects," Appl. Phys. Lett. **126**, 221902 (2025).

[11] J.M. Allred, S. Jia, M. Bremholm, B.C. Chan, and R.J. Cava, "Ordered CoSn-type ternary phases in Co 3Sn 3-xGe x," J. Alloys Compd. **539**, 137–143 (2012).

[12] M. Kakihana, K. Nishimura, D. Aoki, A. Nakamura, M. Nakashima, Y. Amako, T. Takeuchi, T. Kida, T. Tahara, M. Hagiwara, H. Harima, M. Hedo, T. Nakama, and Y. Ōnuki, "Electronic states of antiferromagnet FeSn and Pauli paramagnet cosn," J. Physical Soc. Japan **88**, 014705 (2019).

[13] W.R. Meier, M.-H. Du, S. Okamoto, N. Mohanta, A.F. May, M.A. McGuire, C.A. Bridges, G.D. Samolyuk, and B.C. Sales, "Flat bands in the CoSn-type compounds," Phys. Rev. B **102**(7), 075148 (2020).

[14] B.C. Sales, W.R. Meier, A.F. May, J. Xing, J.-Q. Yan, S. Gao, Y.H. Liu, M.B. Stone, A.D. Christianson, Q. Zhang, and M.A. McGuire, "Tuning the flat bands of the kagome metal CoSn with Fe, In, or Ni doping," Phys. Rev. Mater. **5**(4), 044202 (2021).

[15] H. Huang, L. Zheng, Z. Lin, X. Guo, S. Wang, S. Zhang, C. Zhang, Z. Sun, Z. Wang, H. Weng, L. Li, T. Wu, X. Chen, and C. Zeng, "Flat-Band-Induced Anomalous Anisotropic Charge Transport and Orbital Magnetism in Kagome Metal CoSn," Phys. Rev. Lett. **128**(9), 096601 (2022).

[16] T. Nakatani, N. Suwannaharn, and T.T. Sasaki, "Fabrication and characterization of single-crystalline CoSn($10\bar{1}0$) kagome metal thin films for interconnect applications: Structure and anisotropic electrical resistivity," Appl. Phys. Lett. **127**(20), 203302 (2025).

[17] I. Galanakis, N. Papanikolaou, and P.H. Dederichs, "Applicability of the broken-bond rule to the surface energy of the fcc metals," Surf. Sci. **511**(1–3), 1–12 (2002).

[18] J. Talvacchio, G.R. Wagner, and H.C. Pohl, "YBa2Cu3O7 films grown on epitaxial MgO buffer layers on sapphire," Physica C: Superconductivity and Its Applications **162–164**, 659–660 (1989).

[19] P.A. Stampe, M. Bullock, W.P. Tucker, and R.J. Kennedy, "Growth of MgO thin films on M-, A-, C- and R-plane sapphire by laser ablation," J. Phys. D Appl. Phys. **32**(15), 1778–1787 (1999).

[20] G. Kresse, and J. Hafner, "*Ab initio* molecular dynamics for liquid metals," Phys. Rev. B **47**(1), 558 (1993).

[21] G. Kresse, and J. Furthmüller, "Efficiency of ab-initio total energy calculations for metals and semiconductors using a plane-wave basis set," Comput. Mater. Sci. **6**(1), 15–50 (1996).

[22] J.P. Perdew, K. Burke, and M. Ernzerhof, "Generalized Gradient Approximation Made Simple," Phys. Rev. Lett. **77**(18), 3865 (1996).

[23] P.E. Blöchl, "Projector augmented-wave method," Phys. Rev. B **50**(24), 17953 (1994).

[24] H.J. Monkhorst, and J.D. Pack, "Special points for Brillouin-zone integrations," Phys. Rev. B **13**(12), 5188 (1976).

[25] A.K. Larsson, M. Haeberlein, S. Lidin, and U. Schwarz, "Single crystal structure refinement and high-pressure properties of CoSn," J. Alloys Compd. **240**(1–2), 79–84 (1996).

[26] L. Bengtsson, "Dipole correction for surface supercell calculations," Phys. Rev. B **59**(19), 12301 (1999).

[27] F. Yalcin, and M. Wolloch, "SurfFlow: High-throughput surface energy calculations for arbitrary crystals," Comput. Mater. Sci. **234**, 112799 (2024).

[28] J.F. Nye, *Physical Properties of Crystals, Their Representation by Tensors and Matrices* (Oxford University Press, 1985).